It's just a phase: high-contrast imaging with patterned liquid-crystal phase plates to facilitate characterization of exoplanets

Doelman, D.S.

3 First low-resolution L-band spectroscopy of HR 8799 c,d,e with a vAPP-ALES combination

D. S. Doelman, J. Stone, Z. Briesemeister, A. Skemer, F. Snik, A. Bohn, M. Kenworthy

Context In recent studies, both atmospheric modelling and IFS observations of directly imaged gas giants have focused on y-K band (0.9-2.5μm). However, observations of gas giants in the mid-infrared (3-5 μm) are critical to remove model degeneracies, determine their cloud properties, and give insight in their L-T transition.
Aims We aim to use mid-infrared observations of HR 8799 c, d, and e to provide additional spectral constraints for atmospheric models that are used to infer atmospheric properties.
Methods Using the upgraded mid-infrared ALES spectrograph in combination with the newly installed vAPP coronagraph, we retrieve low-resolution 3.0-4.2 μm spectra (R$\sim$35) of HR 8799 c, d, and e. We compare the obtained spectra with photometric literature values and models reported in literature.
Results The retrieved spectra are consistent with a flat spectrum for all three planets in the observed bandwidth, indicating a low abundance of CH_4. Moreover, the spectra are consistent with previously reported Brα photometry (4.05 μm), strengthening the case for patchy clouds.
Conclusions The retrieved spectra of all three planets are consistent with models with non-equilibrium carbon chemistry and patchy clouds, rather than uniform clouds. This suggests that the HR 8799 planets might be beginning their L-T transition.

3.1 Introduction

Directly imaged exoplanets offer great opportunities to study exoplanet atmospheres. Due to technical limitations, direct imaging has a bias towards young, self-luminous, massive planets at large separations, e.g. HR 8799 bcde (Marois et al., 2008, 2010), β Pic b (Lagrange et al., 2009), 51 Eridani b (Macintosh et al., 2015), PDS 70 bc (Keppler et al., 2018; Haffert et al., 2019) and TYC 8998-760-1 bc (Bohn et al., 2020a,b). These planets have the most favourable contrast with their host star in the thermal infrared (3-5 μm), where the performance of the adaptive optics is also optimal and the thermal background does not yet dominate. The warm gas giants are often compared to field brown dwarfs, as these objects have a similar radius, composition, and also exhibit slow cooling because of the lack of internal fusion (Skemer et al., 2014). Earlier comparisons of photometry of directly imaged planets with measured spectra or modelled spectra of older brown dwarfs showed significant differences (Marois et al., 2008; Morzinski et al., 2015). These differences could only be explained by the presence of disequilibrium carbon chemistry and thicker (patchy) clouds (Bowler et al., 2010; Barman et al., 2011a; Currie et al., 2011; Skemer et al., 2012, 2014). Clouds are patchy when they are non-uniformly distributed and are modelled in literature both as a mix between optically thick and thin clouds, or optically thick clouds combined with cloud free areas. In Barman et al. (2011b) and Marley et al. (2012), the authors suggest that the differences in cloud opacity could be explained by the lower surface gravity of these young exoplanets compared to field brown dwarfs. This was confirmed by comparing young gas giants with low-gravity field brown dwarfs, yielding better fits, e.g. HR 8799 d,e (Bonnefoy et al., 2016), β Pic b (Chilcote et al., 2017) or 51 Eridani b Rajan et al. (2017). These more detailed comparisons are enabled only by the advancements in direct imaging instruments, especially VLT/SPHERE (Beuzit et al., 2019), and GEMINI/GPI (Macintosh et al., 2014) and their integral field spectographs (IFSs) with a combined spectral range spanning the $y-K$ bands (1-2.5 μm). Updated self-consistent models in these wavelength ranges also started to produce better results by taking into account the lower gravity, producing an increase of cloud optical depth (Charnay et al., 2018). Moreover, these models predict a greenhouse effect that shifts the carbon chemical equilibrium, changing the abundances of species compared to similar temperature brown dwarfs with higher surface gravity.

So far, the description of young, self-luminous, massive planets as low-gravity and more cloudy field brown dwarfs is compelling. However, due to inconsistencies in spectra between instruments and different physics in models, it can be difficult to create a true coherent story. For example, 51 Eridani b, a giant planet with many similarities to T-type brown dwarf with strong methane absorption, provides an interesting challenge. When comparing SPHERE and GPI data from Samland et al. (2017) and Rajan et al. (2017), the extracted spectra differ in J and K band, leading to different cloud properties (uniform vs patchy, respectively) and different metallicity (highly super-solar vs solar). Moreover, for the HR 8799 planets both disequilibrium chemistry and the cloud coverage have been disputed. In Currie

et al. (2014), the authors show that for HR 8799 b and c, non-equilibrium carbon chemistry is required, yet only weak evidence for non-equilibrium chemistry is found for HR 8799 d and e. Similarly, both Bonnefoy et al. (2016) and Lavie et al. (2017) find that HR 8799 d,e can be fit well with chemical equilibrium models, in sharp contrast with Skemer et al. (2014) for HR 8799 d,e and Mollière et al. (2020) for HR 8799 e. The same papers disagree differently on the existence of patchy clouds (Skemer et al., 2012; Currie et al., 2014) versus uniform clouds (Bonnefoy et al., 2016; Mollière et al., 2020). We note that patchy clouds or banded cloud structures can generate a linear polarization signal of up to 0.03% and 1.33% respectively, assuming an oblateness of 0 (Stolker et al., 2017). SPHERE/IRDIS measurements of the HR 8799 planets did not recover the planets in linear polarization, despite the unprecedented sensitivity of $\sim 1\%$ (van Holstein et al., 2017). Differences in literature on the retrieved atmospheric properties of the HR 8799 planets can partially be explained by added physics in updated models and the availability of new data. For example, constraining the C/O ratio of HR 8799 e in Mollière et al. (2020) was only possible with the high quality K-band spectrum of the interferometer GRAVITY (GRAVITY Collaboration et al., 2019) and updates of petitRADTRANS (Mollière et al., 2019) to include opacity tables of individual atmospheric absorbers. The update was not included in Wang et al. (2020), where difference in priors significantly changed the retrieved C/O abundance for HR 8799c. However, the exclusion of L and M band data is another factor for explaining in the differences of the retrieved atmospheric properties in literature. In Wang et al. (2020), the retrieved C/O ratio was different when L- and M-band data - compiled by Bonnefoy et al. (2016)- was included, showing that these bands provide additional constraints on the abundances and cloud condition. The focus of modelling has gone toward the $y-K$ band, where VLT/SPHERE, Gemini/GPI, SUBARU/CHARIS (Groff et al., 2017), VLT/GRAVITY and Keck/OSIRIS (Larkin et al., 2006) provided excellent data. Yet, in order to simultaneously pin down T_{eff}, surface gravity, chemistry, and cloudiness, a broad wavelength coverage through the thermal-IR is required (Skemer et al., 2014). Moreover, the L and M-band data presented in Skemer et al. (2012, 2014); Currie et al. (2014) (LMIRcam, non-coronagraphic) can only be explained by modelling patchy clouds for the HR8799 planets, where uniform-cloud models fail to reproduce the 4.05 μm flux, i.e. Bonnefoy et al. (2016); Greenbaum et al. (2018); Mollière et al. (2020). As gas-giants cool and fade, their atmospheres transition from CO-rich and cloudy (L-type), to CH_4-rich and relatively cloud free (T-type). Therefore, it can be expected that gas giants have patchy clouds during the L-T transition, caused by cloud dissipation, and/or clouds sinking below the photosphere of a planet/brown dwarf (Skemer et al., 2014). In addition, the absorption cross-section per molecule of CH_4 peaks between 3-4 μm, while CO peaks between $4.1-5\mu$m (Currie et al., 2014), although the precise shape depends on the pressure-temperature profile. Hence, gaining insight in the cloud properties and C/O ratio during the L-T transition requires thermal-IR observations. Another reason for thermal-IR observations is that planets with lower masses, elderly planets, and cold-start planets will all be cooler than the planets currently detected with direct imaging (Fortney et al.,

2008). These cooler planets emit most of their light in the thermal-IR, where the contrast is also most favourable with respect to the host-star. To summarize, thermal-IR observations are necessary to remove model degeneracies in gas giants, to improve the understanding in their L-T transition, and to detect cooler planets. The Arizona Lenslets for Exoplanet Spectroscopy (ALES) is an adaptive optics-fed integral field spectrograph with sensitivity out to 5 microns (Skemer et al., 2015, 2018) and is installed at the Large Binocular Telescope (LBT). ALES was specifically designed to provide insight in the L-T transition of gas giants. The updated ALES has a main mode with a square field of view of $\sim$2.2 arcseconds with a spectral resolution of $\sim$35, spanning the $2.8 - 4.2$ μm range. Other modes have different spectral resolutions (R = 20-150) and spectral coverage spanning $2 - 5$ μm. Additionally, LBT/LMIRCAM (Wilson et al., 2008) has been upgraded with a double-grating 360-degree vAPP (dgvAPP360) coronagraph (Snik et al., 2012; Otten et al., 2017; Doelman et al., 2020), suppressing the stellar diffraction halo by multiple orders of magnitude over the full $2 - 5\mu$m bandwidth. The vAPP coronagraph in LMIRCAM can also be used for the ALES spectrograph. This combination of ALES+vAPP has several advantages. First, using the same coronagraph over the full wavelength range makes it easier to compare data taken in different instrument modes. Second, the diffraction structure of the vAPP point-spread function (PSF) is more stable as function of wavelength than that of focal-plane coronagraphs. Focal-plane coronagraphs have a changing transmission of the focal-plane masks near their inner working angle, which, combined with the wavelength dependence of atmospheric dispersion correction, changes the performance with wavelength. The vAPP PSF is only shifted while keeping the same shape, allowing for improved spectral differential imaging (SDI) (Racine et al., 1999). Third, being a pupil plane coronagraph, the vAPP generates a PSF that is independent on the location in the field of view (FOV). Therefore, all stars and companions have the identical PSFs, in contrast to focal-plane coronagraphs. Identical PSFs respond the same to variations in Strehl, making the stellar PSF a good photometric reference, especially in the thermal-IR where fast imaging is standard due to the high thermal background. Fourth, with the absence of a focal-plane mask and the PSF being independent on the location in the FOV, it is no longer necessary to accurately align the PSF on focal-plane masks. This reduces overhead at the beginning of an observing sequence, as well as reducing the complexity for chopping and nodding.

In this paper, we present the first low-resolution spectra of HR 8799 cde in the 3.5-4.1 μm range using the ALES/vAPP combination. First, we characterize the vAPP performance in section 3.2. Section 3.3 summarizes the observational data and data reduction. We show the retrieved spectra in section 3.4 and discuss them in section 3.5.

3.2 Characterization of the dgvAPP360.

The dgvAPP360 in LMIRCAM was installed early September 2018. The design and first-light results are presented in Doelman et al. (2020). In this paper we show that the double-grating vAPP is operating as expected, and that it produces a single coronagarphic PSF in contrast to standard gvAPPs (Otten et al., 2017). In addition, observations of the disk PDS 201 in L'-band (3.41 - 4.00 μm) using this vAPP show that the vAPP has an improved sensitivity of a factor two compared to non-coronagraphic imaging in the regions closest to the star (450-800 mas) (Wagner et al., 2020). Yet, the performance and vAPP properties are not fully characterized because of the contribution of the disk. In this section, we characterize the vAPP by studying the PSF using the internal source.
First, we image the PSF using LMIRCAM to explore the star light suppression in the dark zone of the vAPP. We use the internal source of LMIRCAM and the installed L-band filter (2.82 - 4.21 μm) [1]. We take 30 images of 0.5 seconds integration time and subtract the average dark of 10 images with the same integration time. We median-combine the all images, and the final PSF is shown in the top left of Fig. 3.1. The almost vertical stripes present in the image are created by the internal source of LMIRCAM and are caused by light leaking around a pin hole mask. These stripes are not present in on-sky data, and are ignored in the further analysis of the PSF. We select a D-shaped region on the left side of the PSF to estimate the raw contrast. Moreover, we mask two ghosts, in this dark zone and two features that are aligned with the stripes to obtain an accurate estimate of the raw contrast of the vAPP. The masks are shown on the top right of Fig. 3.1. The flux is averaged azimuthally in half annuli and normalized on the peak flux of the PSF. In addition, we simulate a PSF with the same plate scale and bandwidth, assuming a uniform spectral profile, using `HCIPy` (Por et al., 2018). The measured raw contrast and the raw contrast of the simulated PSF are shown in the bottom panel of Fig. 3.1. The raw contrast reaches the noise floor of 5.8×10^{-5} ($\Delta m = 10.6$) at a separation of 470 mas, calculated at 3.9 μm. Closer in, the contrast is reduced by 1-2 magnitudes compared to the theoretical curve, likely due to some low-order aberrations. The theoretical inner working angles and outer working angles for the vAPP are presented in table 3.1. The noise floor, dominated by the thermal background, is given by the average flux between the two bright rings of the PSF (3.0"-3.4"), using half-annuli. We conclude that, within the limitations of the measurement, the coronagraphic performance of the vAPP is as expected.
The double-grating vAPP has two separate liquid-crystal layers, an additional glue layer and an extra substrate compared to a standard gvAPP (Doelman et al., 2017, 2020). These additional layers lead to extra absorption, specifically in the 3.24-3.5 μm range, where both the liquid-crystal molecules and the glue molecules have an absorption feature from carbon-carbon bonds (Otten et al., 2017). We note that

[1] `http://svo2.cab.inta-csic.es/svo/theory/fps3/index.php?id=LBT/LMIRCam.L_77K&&mode=browse&gname=LBT&gname2=LMIRCam#filter`

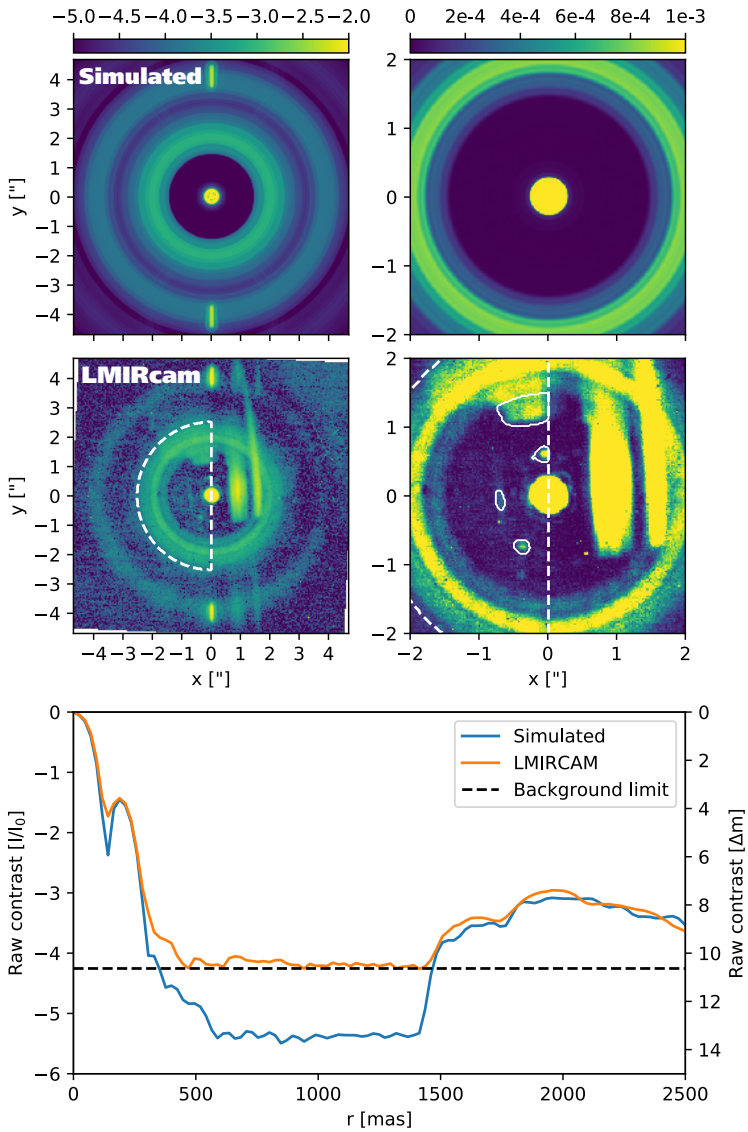

Figure 3.1: Images and the raw-contrast curve of the L-band point-spread function of the vAPP in LMIRCAM using the internal source. The stripes are created by the internal source and are not present in on-sky data. The raw contrast was calculated by averaging half-annuli in the marked D-shaped region, omitting the regions marked by the solid line in the top right figure. These regions contain ghosts and stripes from the internal source.

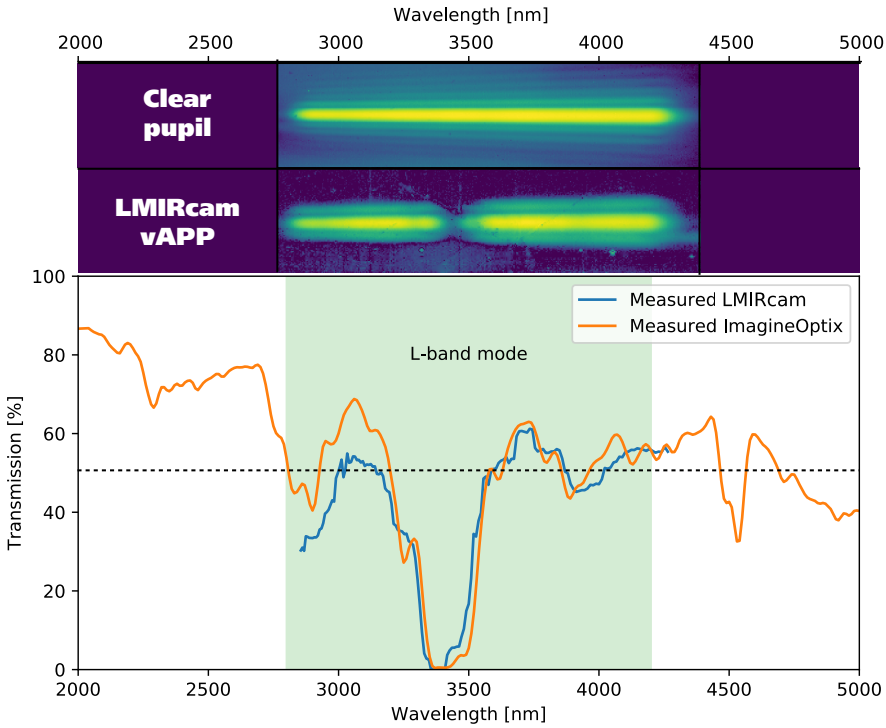

Figure 3.2: Transmission measurements of the vAPP in the 2.8-4.2 μm range using a grism to disperse the vAPP and non-coronagraphic PSF.

Table 3.1: Theoretical inner working angles (IWAs) and outer working angles (OWAs) as function of wavelength, λ. The OWAs larger than the ALES field of view are in italics.

λ (μm)	2.0	2.3	2.8	3.3	3.9	4.2
IWA (mas)	143	200	250	278	300	357
OWA (mas)	793	1110	*1388*	*1547*	*1666*	*1983*

the Annular Groove Phase Mask (AGPM) coronagraph also has this absorption feature because they are made from diamond (Defrere et al., 2014). Because these features are in the spectral range of ALES, we conduct an experiment to mesaure the impact. We disperse the coronagraphic (vAPP) PSF and non-coronagraphic (clear pupil) PSF using a grism in tandem with the *L*-Spec filter, using only the left aperture (SX) of the internal pupil mask. The dispersed PSFs are displayed in Fig. 3.2. In addition, we obtain narrow band images at 2.9 μm, 3.3 μm, 3.5 μm, and 3.9 μm that are used for wavelength calibration. Because the pupil selection mask is in the same filter wheel as the narrow band filters, the narrow band images are the coherent sum of both pupils, creating Fizeau fringes. We remove this effect for our wavelength calibration by summing the flux in 100 pixels in the fringe direction. We fit a Gaussian to the one-dimensional sum of each wavelength to retrieve accurate centroids. We then use the centroids to calculate the wavelength solution of the dispersion.
Calculating the transmission of the vAPP is complicated by the difference in intrinsic Strehl between the two PSFs. The vAPP has an intrinsic Strehl of 46% and the PSF core is slightly broadened due to the apodization by the vAPP in the pupil plane. We retrieve the actual throughput by forward modelling both PSFs for the full bandwidth. For continuous wavelength coverage, we generate a wavelength-scaled PSF every 2 pixels in the image, corresponding to an average spectral resolution of 10 nm. The model PSF is the incoherent sum of all individual PSFs with an individual scale factor. We minimize the difference between the simulated and measured PSF by changing these scale factors, thereby retrieving the true input spectrum. The final transmission is the optimized vAPP spectrum divided by the non-coronagraphic spectrum, and is shown in Fig. 3.2. We compare the results with the transmission that is measured by the manufacturer. The curves are in good agreement except for the transmission between 2.9 and 3.2 micron. It is unclear what causes the difference of more than 10% in this spectral bin, compared to the LMIRcam average transmission of 47%. A significant fraction of the spectral band is unavailable when using the vAPP because of the absorption feature. Specifically, the absorption is centered on a spectral feature of CH_4. While this inhibits the detection of methane in the atmospheres of L-type gas giants, cooler gas giants with more CH_4 will have a measurable spectral slope between 3.5-4.1 μm, where the average transmission of the vAPP is 51%.

3.3 Observations and data reduction

We observed HR 8799 on 2019 September 18 for 1 hour 53 minutes with the LBTI/ALES instrument in combination with the vAPP coronagraph. Only the left-side telescope fed the ALES instrument at the time of observation, the other side was feeding a different instrument. We used the *L*-band mode of ALES, spanning $2.8 - 4.2$ μm, with a spectral resolution of ~ 35 (Skemer et al., 2018). We acquired 1300 frames on-target with an integration time of 3900 milliseconds per frame, for a total of 1 hour 24 minutes. The conditions were stable with a seeing

between 0.8 and 1.1 arcseconds, and the derotator was switched off, yielding a total field rotation of 85°.64 through meridian crossing. In addition, we take a total of 99 background frames, where the first 13 were taken after 100 science frames and the other 86 directly after the science sequence. This unconventional observing sequence without beam switching increases the time on-source and minimizes overhead time, yielding an on-target observation efficiency of 93%. The downside of this method is a higher photon noise in the background estimates.

3.3.1 Spectral cube extraction

A lenslet-based integral field spectrograph images the focal-plane onto a microlens array, followed by a dispersing element. Raw images from this instrument contain a spectrum for every focal-plane location that corresponds to individual lenslets. To extract the images as function of wavelength (= spectral cube), we use a data reduction pipeline called Methods for Extracting ALES Data (`MEAD`) (Briesemeister et al., 2018). This pipeline cleans up the raw images (e.g. dark subtraction, pixel flat-fielding), calculates the focal-plane geometry to correct displacements between the prism and the lenslets, implements the wavelength calibration, and maps every light-sensitive pixel to a weight in the created data cube. We inspect the extracted cubes and find two unusual properties of the data. First, we see that the background is highly variable as function of wavelength, specifically at the lower end of the wavelength range. This indicates that there is a light leak present in the ALES instrument that contributes to the thermal background. While the light leak is additive, and can thus be removed through standard background subtraction, it contributes to a structured photon noise pattern on the detector. Second, we find that during the observation sequence the PSF moves compared to the background in a u-shape. This u-shape is $\sim$ 35 mas (=1 spaxel) in the x-direction and $\sim$ 70 mas in the y-direction, while the frame-to-frame jitter is $\sim$ 4 mas. A known source of PSF movement in ALES is the lenslet array, which moves due to flexure of the instrument with telescope pointings. The movement of the PSF on the detector is correlated with airmass, suggesting that flexing is indeed a contributor. However, the movement of the lenslets has not been known to exceed one spaxel, and perhaps other factors contribute as well. We note that any PSF movement prior to the lenslets is not affecting the coronagraphs performance because the vAPP is a pupil-plane coronagraph. PSF movement on the focal-plane mask of coronagraph's like the AGPM would reduce their performance. As a final step, we bin the data per four frames in time by averaging, reducing the number of cubes from 1300 to 325.

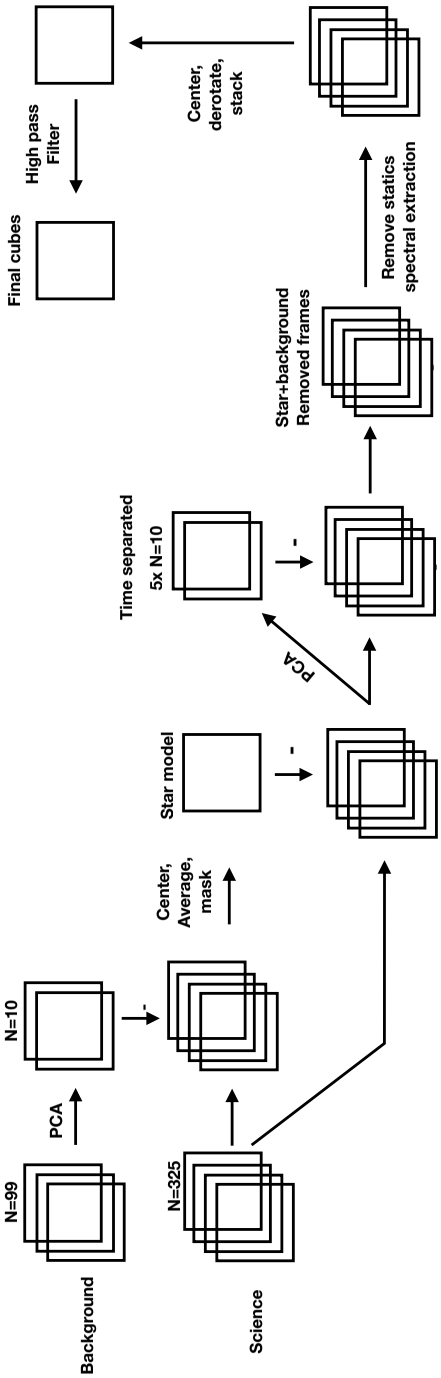

Figure 3.3: Flowchart of the data-reduction method.

3.3.2 Data reduction

Most conventional data reduction algorithms remove the background from the frames at this point. However, removing the thermal background from the science data using only the 99 background frames is suboptimal. Any residuals in the background-subtracted frames that are static, will not be static compared to the shifting frame of reference of the PSF. Techniques like angular differential imaging (ADI) (Marois et al., 2006) will not capture these structures and they will carry over to the final frames. Yet, the background is present in every science image, of which there are 1300 before binning. Besides this background, the science frames also contain the stellar and planetary PSFs. Because the planets move across the detector with the parallactic angle, they can easily be removed from the background estimate. We can mask their predicted locations, such that their flux is not influencing the background estimates. The star constitutes a larger problem, as possible quasi-static speckles or ghosts will contaminate the estimated background. In addition, the background on the stellar PSF location is inaccessible, which makes accurate stellar photometry impossible.
We introduce a combined method where we model the star and background separately and subtract them from all frames for each wavelength. A flowchart of the method is shown in Fig. 3.3. We start by subtracting the 99 background frames from the science data to create a stellar PSF model. While these background frames introduce noise at the planet locations, the background noise is much lower than the stellar photon noise. Therefore, an accurate model of the stellar PSF can be extracted by centering and co-adding the background subtracted frames. We create a mask to select features that are significant and co-moving with the star, i.e. a ghost and ringing from the spectral cube extraction. The ringing could be a combined effect from electrical ghosts by inter-channel capacitive coupling (Finger et al., 2008) and the cube extraction. The data is also clipped to remove all features that are less than 2σ compared to the background outside of the mask. An example of the PSF model for a single wavelength is shown in Fig. 3.4. Removing the stellar PSF from the science data using this PSF model is now straightforward. We fit a decentered PSF model to background subtracted data frames for each wavelength, retrieving the stellar PSF intensity and the science frames without the stellar PSF.
After masking the planets, we can model the background from the star-subtracted science frames. To minimize self-subtraction, we select for every frame the frames separated in time by 30 minutes and calculate 10 PCA components from this selection. We optimally subtract these components, such that the residuals in the frame are dominated by the photon noise of the star and background. This method of background subtracting results in cubes with a subtracted star and background, where the background is calculated from the science frames themselves. Now, we can check if this method indeed reduces the background noise compared to simply using 10 PCA components of the 99 background frames. By subtracting 10 PCA components from the raw data for both methods, we compare the standard deviation of the residuals after masking the star. Between 2.9 μm and 4.2 μm,

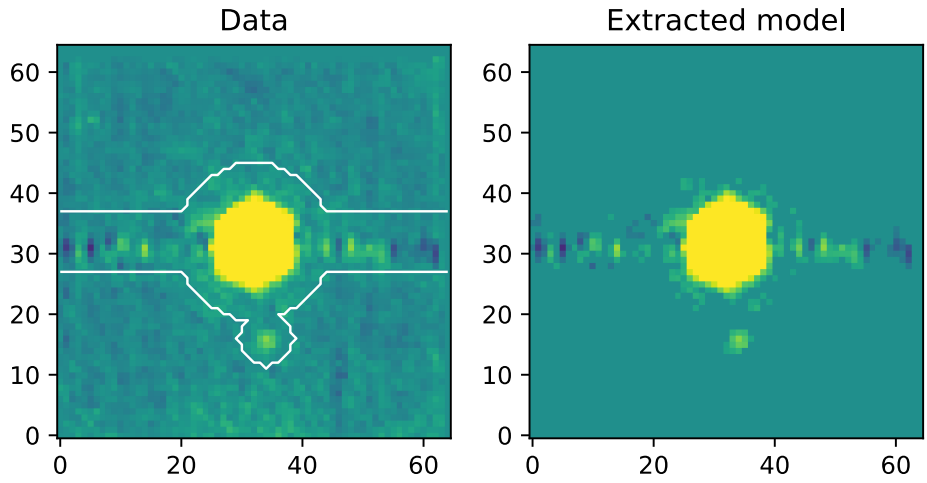

Figure 3.4: *Left:* Background-subtracted PSF at 3.55 μm, using 10 PCA components of the 99 background frames. Residual structures indicate the presence of a ghost, some speckles, and a horizontal oscillating structure. *Rigth:* Same as left, but clipped at 2σ inside the area of a mask, indicated by the white lines left image.

we obtain a reduction of 10% in the standard deviation of the residuals using the data as a background estimate. While this would be less than what could expected from photon noise alone, we proceed with the science data background estimate. We inspect the star- and background-subtracted frames for residual structure by averaging them in time and wavelength. We find that the residuals are not well described by purely Gaussian noise, but contain structures that are column and row specific and vary in time, see Fig. 3.5. The structures are faint (1-10 counts) and originate from the spectral cube extraction. Each pixel in the spectral cubes correspond to a spaxel in the raw data, which are separated by multiple pixels on the detector. Discontinuities in rows and columns are therefore expected. We characterize these discontinuities by fitting polynomials of the third order to each row and column, which are shown in Fig. 3.5. A third order polynomial is low-order enough compared to the 65 pixels that it is minimally affected by planet signal. Yet, we mask the star with an 18 pixel circular mask and the planets with a 5 pixel circular mask and remove those pixels from the fit. Using a Kolmogorov-Smirnov test we verify that both the before and after distributions are non-Gaussian, however we find that the average of the noise distribution is now consistent with zero and the standard deviation is reduced by 10%. We note that the polynomial background fit has a large number of variables for the full image, but it was the only method that captured the behavior of this phenomenon. Combined with the stellar PSF removal and the background removal, the row and column fits remove most structures present in the data in a way that minimizes self-subtraction of planets. The authors would like to *reiterate* that this unconventional data reduc-

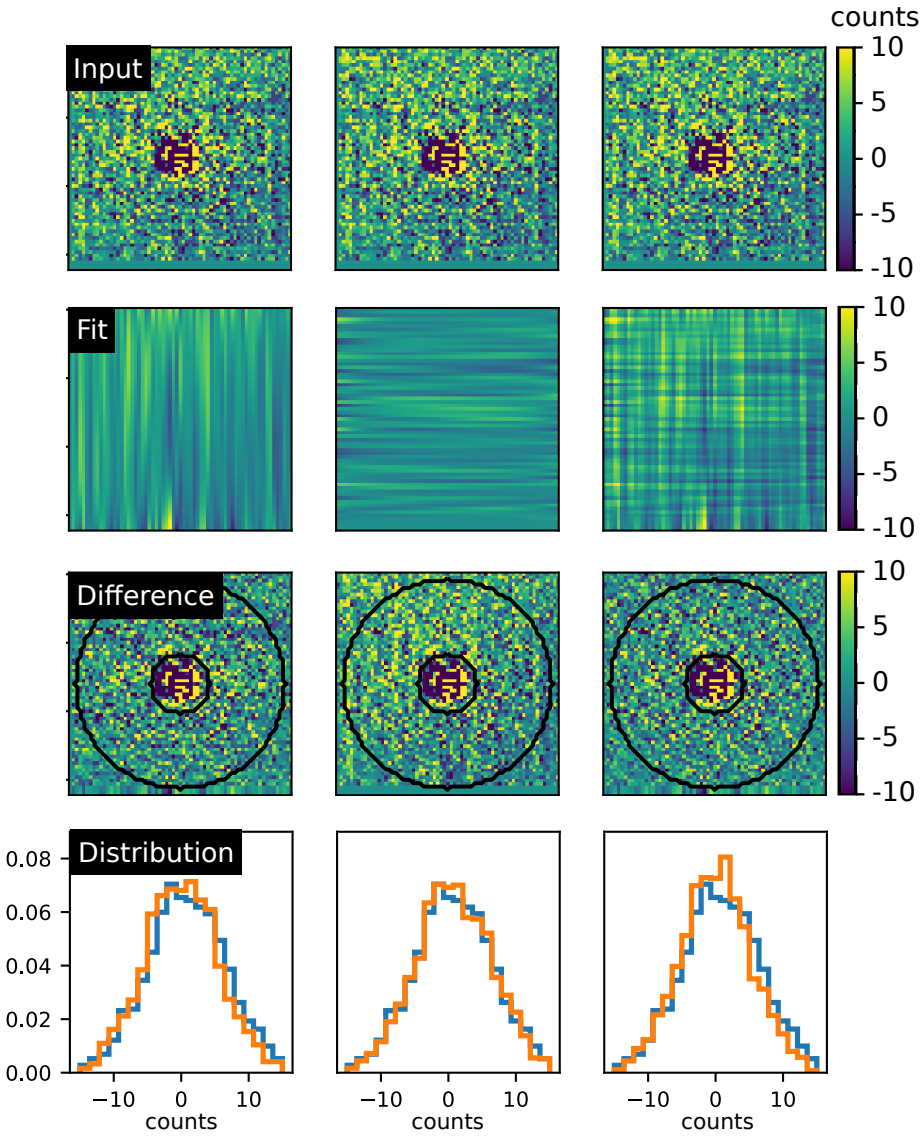

Figure 3.5: Removal of row and column discontinuities by fitting a third-order polynomial to every row and column.

tion method is required because of the low number of available background frames and the movement of the stellar PSF. ADI centered on the star would not be good at characterizing the static structures of the background, including the row and column discontinuities.
We center and derotate the background subtracted cubes and median stacking them in time. A final step is a high-pass filter, where we remove global structures on the background by removing a Gaussian smoothed frame for each wavelength in the final cube. The Gaussian has a standard deviation of 5 pixels (FWHM = 11.8 pixels) and we mask the locations of the HR 8799 planets and the star.

3.3.3 Spectral extraction

The data reduction aims to minimize self-subtraction. However, self-subtraction is still non-zero and it is wavelength-dependent. To extract the final spectra, we negatively inject planets at the locations of the HR 8799 planets in the extracted data cubes. The injected planets are copies of the stellar PSF at each wavelength. The raw cubes are reduced using the method described in Fig. 3.3. We optimize their location and amplitude by evaluating the Hessian at the planet location in a circular aperture with a diameter of 7 pixels. The Hessian is a measure of the curvature of the image surface, which is minimal when the planet is completely removed (Stolker et al., 2019). To evaluate confidence of the retrieved spectra we apply bootstrapping to the data reduction method, selecting 325 frames at random from the data for 50 times in total. The fluxes of the planets for each wavelength are retrieved using aperture photometry, rather than fake planet injection, as the data reduction method is rather computationally expensive. Assuming that the self-subtraction is similar for all iterations, the distribution of retrieved amplitudes should be a good approximation of the distribution with negative planet injection. From this posterior distribution of planet fluxes, we take the standard deviation as the 1σ error bars. Moreover, we bin the data between 2.99 and 3.17 μm and 3.17 and 3.36 μm in single wavelength bins to retrieve two photometric points for wavelengths short of the vAPP aborption feature. The negative planet is injected for all spectral bins separately, however, the final evaluation of the Hessian is done on the median combined images in the wavelength bins. Bootstrapping with the same parameters is applied to find the error bars on these spectra as well.
We perform the true flux calibration of the spectra using the SED analyser VOSA (Bayo et al., 2008). We fit a BT-Settle model to the SED of the host star and retrieve a temperature of 7200 K, $\log(g) = 4$ $\log(cm/s^2)$, a metallicity of 0.5, an $\alpha = 0$ and and a multiplicative dilution factor of 6.416e-19. This BT-Settle model is used to calculate the true flux of the host star in every wavelength bin. We multiply the relative flux of HR 8799c,d,e with the stellar flux to retrieve the final spectra.

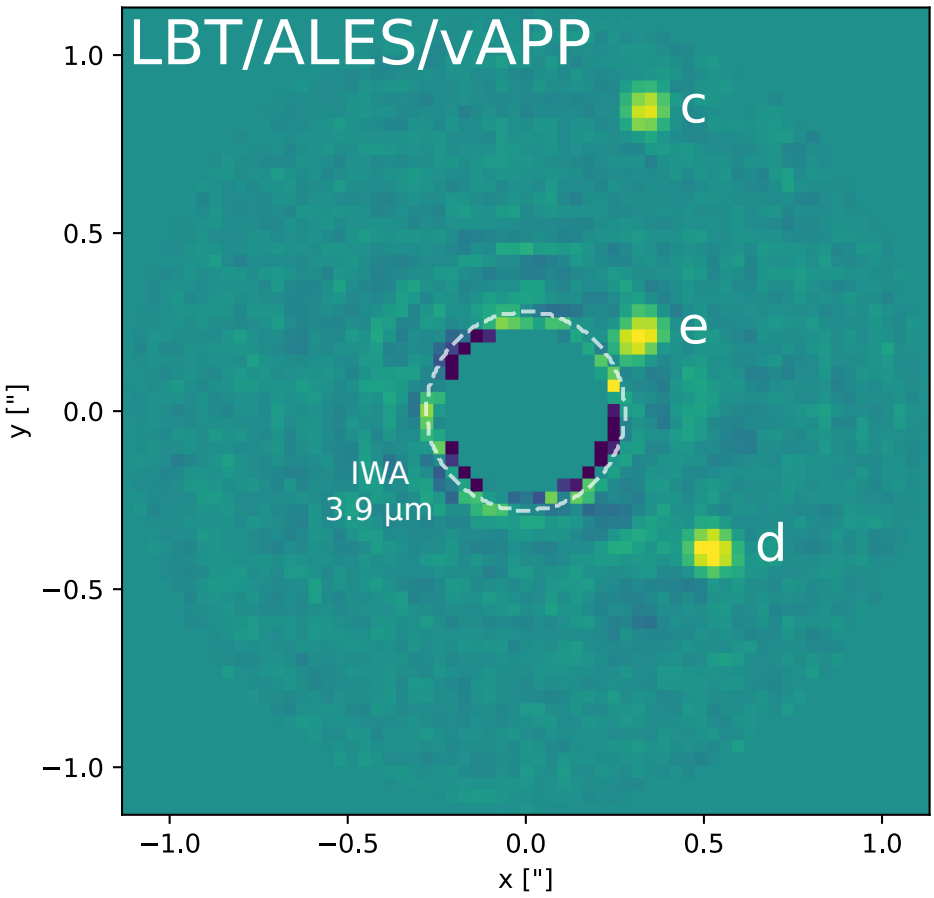

Figure 3.6: LBT/ALES image of HR 8799 cde using the vAPP coronagraph. The final image is the combination of the individual wavelength slices between 3.55-4.25 μm. North is up, East is left. The images are 2.2" across.

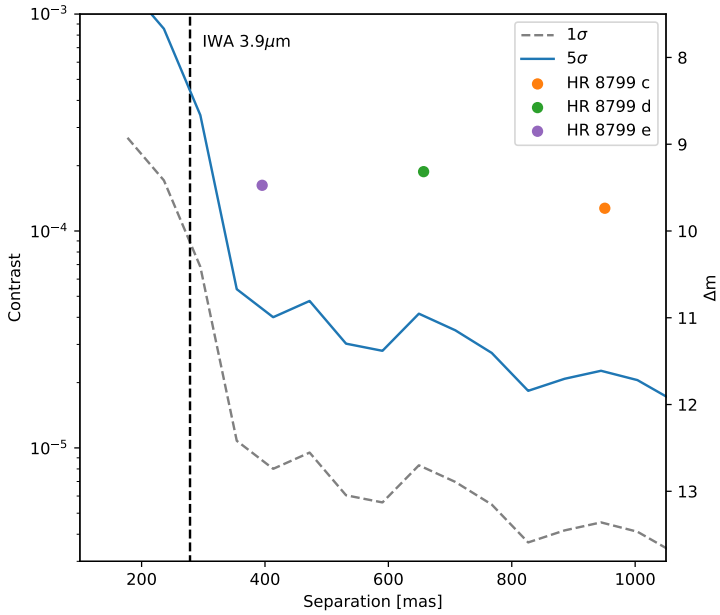

Figure 3.7: Planet-to-star contrast for the LBT/ALES as a function of angular separation.

3.4 Results

Using the combination of ALES with the dgvAPP360, we recover HR 8799 c, d, and e. We note that HR 8799 b is outside of the field of view of ALES. We optimally combine the data between 3.5 μm and 4.2 μm to maximize the signal-to-noise ratio, where the throughput of the vAPP is highest. The final image is shown in Fig. 3.6, where all three planets are clearly visible. Only at the location of HR 8799 e there are some residuals from speckles, while the residuals at the locations of HR 8799 c and d are dominated by the thermal background. We calculate the post-processed contrast using aperture photometry. We compare the standard deviation in the sums of the flux in subapertures with a diameter of $1.7\lambda/D$ for a given angular separation. The resulting contrast curve is shown in Fig. 3.7, and quickly reaches a noise floor beyond the inner working angle. HR 8799 c, d, and e are detected with a signal-to-noise ratio of 29, 25 and 19 respectively.
The retrieved spectra of the inner three HR 8799 planets and literature values for these wavelengths are compiled in Fig 3.8. Interestingly, the retrieved spectra of HR 8799 c, d, and e are almost equivalent, given an absolute offset. They are almost completely flat and featureless over the used bandwidth of the ALES

spectrograph. HR 8799 d is the brightest, followed by HR 8799 e, and HR 8799 c. We significantly detect HR 8799 c and d between 2.99 and 3.35 μm, with fluxes that are comparable with the recovered fluxes for wavelengths longer than 3.5 μm. No significant detection was made between 3.35 μm and 3.5 μm due to the absorption of the vAPP coronagraph. The retrieved spectra of HR 8799 c and e are consistent with the reported literature values. On the other hand, HR 8799 d shows significant deviations of compared to the values reported in Skemer et al. (2014), up to a factor of 3. We will discuss this further in section 3.5.1.

3.5 Discussion

3.5.1 Data reduction and the increased flux of HR 8799 d

We find that the retrieved spectra of HR 8799 c and e are consistent with literature values, and deliver a complementary view of the system. The spectra show a channel-to-channel variation that is often larger than the bootstrapped error bar. This is curious as the spectral extraction is done at a higher spectral resolution ($R \sim 200$) than the spectral resolution of the spectrograph ($R \sim 35$) (Skemer et al., 2018). Systematic errors from the cube extraction are the likely cause of the channel offsets. More importantly, the recovered spectrum of HR 8799 d shows a larger flux than the reported L-band fluxes. As the recovered fluxes of the other two planets are consistent with literature, it is not likely that it is merely a scaling issue. Moreover, being the middle planet of the three, it is implausible that algorithmic mechanisms like self-subtraction would cause this difference. It is more likely that offsets are introduced either during the cube extraction, the star subtraction, or that the increase in flux is astronomical of origin. These three possibilities would have a different time dependency, meaning that the flux of the planets would change in time in a different way. We explore the time variability of the three planets by combining 22 minutes of data and the wavelength channels between 3.6 and 4.1 μm into a single photometric point. The resulting five photometric points for each planet are shown in Fig. 3.9. The error bars are determined by bootstrapping the 22 minutes of data 50 times and taking the standard deviation of the planet flux. Flux variations from varying AO performance of sky transmission are corrected by photometry of the stellar PSF. It is clear that the behavior of HR 8799 c and e is again different from the behavior of HR 8799 d, which is not relatively constant but decreases by a factor of 2 over the observing time.

It is worthwhile to note that HR 8799 d is on a different quadrant on the detector than HR 8799 c and e. The current extraction does not use a lenslet flat, accounting for non-uniformity in the illumination of the lenslets. Moreover, field dependent aberrations, such as astigmatism, can change the shape of a PSFlet to align with or be orthogonal to the dispersion direction of the grism. Not only would this lead to a change in the effective spectral resolution, but depending on the width of the mask used for spectral extraction, could lead to flux variations.

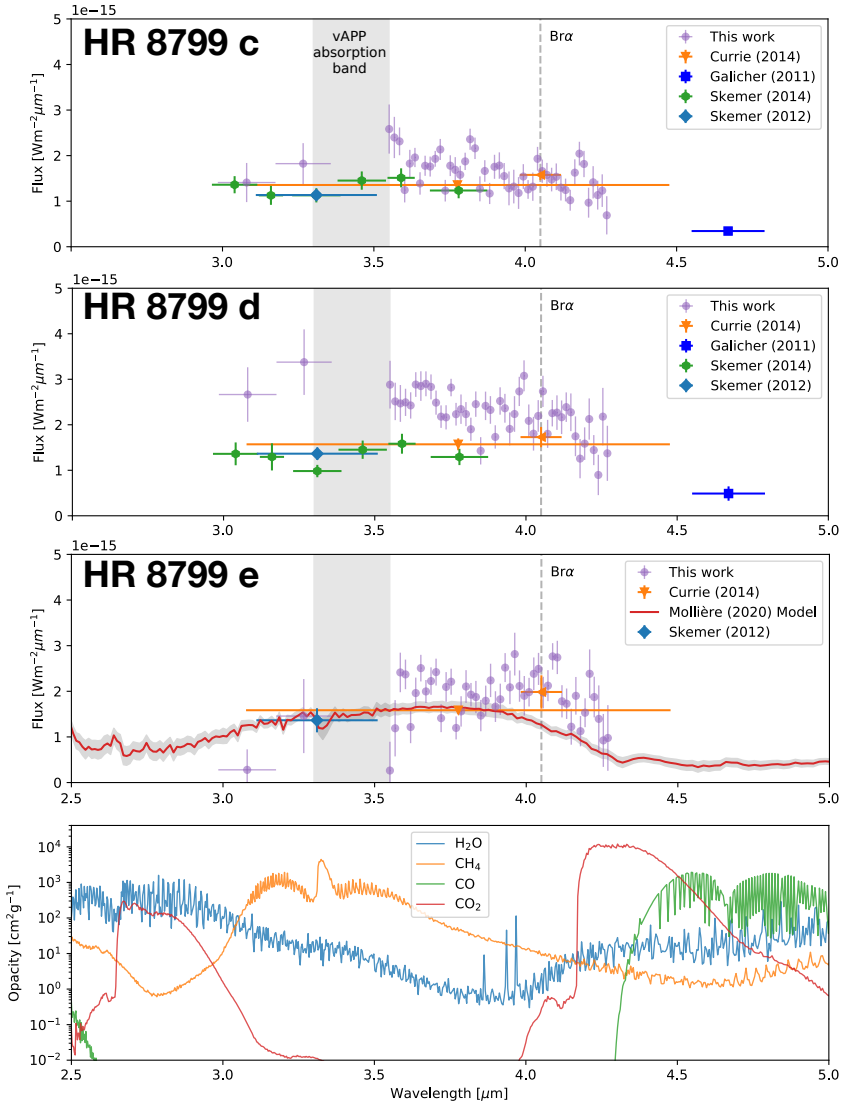

Figure 3.8: Spectra recovered with negative planet injection for HR 8799 cde, showing flux at 10 pc. We use the data 3.3 μm magnitudes from Skemer et al. (2012), the different narrow-band magnitudes from Skemer et al. (2014), the broad L'-band and Brα magnitudes from Currie et al. (2014), and the M-band magnitudes from (Galicher et al., 2011). In addition, we add the best-fit model for HR 8799 e from Mollière et al. (2020). The bottom panel shows the opacities of H_2O, CH_4, CO, and CO_2 in the same wavelength range, calculated with PetitRADTRANS for a temperature of 1200 K and a pressure of 1 bar. (Mollière et al., 2019).

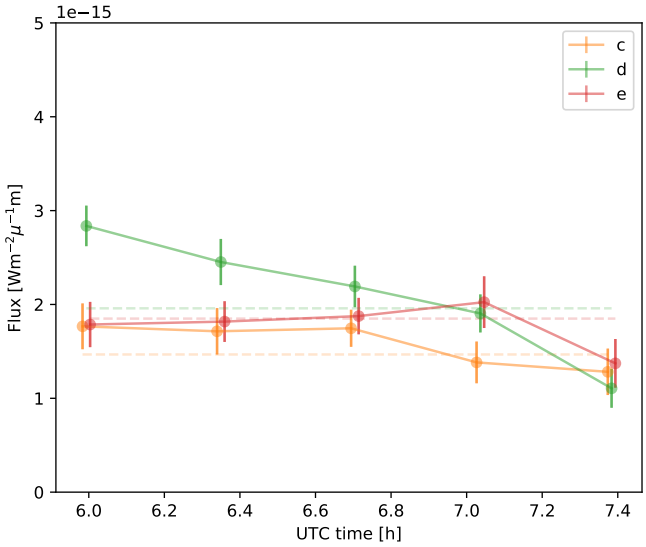

Figure 3.9: Retrieved flux of HR 8799 c, d and e between 3.6 and 4.1 μm for five different time bins spanning 22 minutes.

Such effects have not been characterized, and are currently not captured in the `MEAD` pipeline. However, this is unlikely to cause a factor of 2 in flux variation for a single quadrant of the detector.
Another possibility is the star subtraction, where we subtract average PSF structures. The horizontal oscillating structure has a similar magnitude as the HR 8799 planets and HR 8799 d passes through this structure in the first 22 minutes of the observation run. HR 8799 e passes through some of the PSF structures that look like speckles, yet the photometry is the most stable. It is likely that these structures affected the photometry of HR 8799 d and e, although this can not be responsible for the total decline in the flux of HR 8799 d after the first 22 minutes. HR 8799 c is not affected by any stellar subtraction, yet it also shows a decline during the last 44 minutes. The star subtraction can therefore not be solely responsible for the flux offset of HR 8799 d. We note that not subtracting these PSF structures would also lead to flux variations of the planets. An improved PSF characterization and subtraction would be beneficial to the spectrum and the variability measurements. We reject the possibility that the increased flux of HR 8799 d with respect to literature values is caused by intrinsic variability of the planet. While some variability is expected for a cloudy atmosphere, this would not be very strong in the L-band (Lew et al., 2020a). Therefore, it can not explain a variation of a factor 2 in flux between our measurements and the Skemer et al. (2014) data.

3.5.2 Implications of the common flat and featureless spectra

The ALES spectrograph covers 2.8-4.2 μm, which contains only a few features from the most abundant molecules, shown in the bottom panel of Fig. 3.8. Most prominent is the methane band (3.0-4.0 μm), which has a peak opacity at 3.3 μm. At one edge is an H_2O band (2.5-3.0 μm), while just beyond the other edge there is a CO absorption band (4.3-5.1 μm). It is therefore expected that for T-type gas giants their spectrum in the ALES band is dominated by CH_4 absorption, while the CO dominated atmospheres of L-type gas giants do not show a lot of structure. As noted before in Skemer et al. (2014), the spectra of HR 8799 c and d relatively flat at between 3 and 3.8 μm wavelengths, indicating that the atmospheres are still CO dominated. Photometry of HR 8799 e at 3.3 μm could only be explained by carbon disequilibrium chemistry, with lower CH_4 abundances (Skemer et al., 2012) compared to field brown dwarfs, which was later confirmed by Mollière et al. (2020) using the radiative transfer code PetitRADTRANS. It is therefore expected that HR 8799 c, d, and e only have a weak methane absorption feature, which is in agreement with our data. A common feature of our retrieved spectra of the three HR 8799 planets is that they are almost constant in flux between 3.0 and 4.0 μm. Due to the absorption band of the vAPP coronagraph it is not possible to further constrain the methane absorption.

For wavelengths longer than 4.0 micron we detect planet fluxes that are consistent with their 3.5-4.0 micron flux. Moreover, our data at 4.05 micron (Brα) agrees with the values reported by Currie et al. (2014) for all three planets, showing that the flatness of the spectrum beyond 4 μm is likely real. This flatness of the spectrum beyond 4 μm is interesting because our data for HR 8799e clearly shows a discrepancy with the uniform-cloud PetitRADTRANS model (Mollière et al., 2020) for these wavelengths. This discrepancy between models and the fluxes at these longer wavelengths has been reported before (Madhusudhan et al., 2011; Bonnefoy et al., 2016). A solution for the disagreement between the flux in the Brα filter and simulated spectra has been used as a key argument in favour of patchy clouds (Skemer et al., 2012, 2014; Currie et al., 2014). Patchy cloud models have a flatter spectrum beyond 4 μm, extending to the CO absorption band at 4.3 μm similar to our data. The slope and total flux in this wavelength range does depend on the implementation of patchy clouds, which can be a partial cloud cover with cloud-free patches or patches with clouds at different temperatures (cloud mixing). Cloud mixing gives better results (Skemer et al., 2014), but is not self-consistent. The cloud models are not good enough to retrieve atmospheric properties, but they are promising for explaining our HR 8799 c, d, and e spectra.

The inconsistency of modelled and measured flux beyond 4 μm is not the only indication for the existence of patchy clouds. Brown dwarfs show photometric variability that could be explained by a heterogeneous cloud coverage (Apai et al., 2013; Lew et al., 2020b,a). In addition, the luminosity of gas giants and their

colors are in tension with each other, resulting in models of gas giants with planet radii that are not physical, i.e. < 1 M_J (Bonnefoy et al., 2016; Greenbaum et al., 2018). Electron degeneracy pressure prevents the radii from decreasing further than this limit. A solution is again given by patchy clouds, such that the planet emits non-isotropically with brighter and darker patches, like the bands of Jupiter. The bright patches dominate the shape of the spectral energy distribution, while the total emitting area is smaller, allowing for a physical planet radius (Skemer et al., 2012) that matches the luminosity.
New observing methods or new instrumentation have provided multiple indications of patchy clouds for gas giants in their L-T transition, and highlighted the discrepancy between models and and the spectra of gas giants. In the near future the James Webb Space Telescope will deliver more stable photometry at longer wavelengths, and high-resolution spectroscopy combined with coronagraphy will provide more insight the presence of molecular species in atmospheres of gas giants (Mawet et al., 2016; Otten et al., 2020). To fully understand the data and its implications for the atmospheres of young massive exoplanets or field brown dwarfs, a next step would be to develop atmospheric models that include patchy clouds.

3.6 Conclusions

We report on the first science results of the upgraded ALES spectrograph, with a spectral higher resolution(R$\sim$35) and a new double-grating vAPP coronagraph with a 360 degree dark zone. We characterize the coronagraphic performance, reaching a raw contrast of 3×10^{-4} at 300 mas at 3.9 μm and the background limit (5.8×10^{-5}) at 470 mas. Using the upgraded ALES in combination with the broadband double-grating vAPP, we recover these three planets between 3.0 and 4.25 μm and obtain the first low-resolution L-band spectra of HR 8799 c, d, and e. We find that the spectra of all three planets are similar and flat in these wavelength ranges. The recovered spectra show no significant flux decrease beyond 4 μm and find that the planet fluxes at Brα (4.05 μ) are consistent with literature values. So far, only models implementing a heterogeneous cloud coverage can explain this excess flux, which strengthens the case that the atmospheres of HR 8799 c, d, and e do not contain uniform clouds, and perhaps have started their L-T transition. We detect no significant methane absorption, although this is not well constrained by our data as an absorption band of the vAPP coronagraph obscures the 3.3 micron feature. The lower abundance of methane compared to field brown dwarfs of similar temperature is consistent with previous findings, indicating that disequilibrium chemistry plays a role for all three planets.

Bibliography

Apai, D., Radigan, J., Buenzli, E., et al. 2013, The Astrophysical Journal, 768, 121
Barman, T. S., Macintosh, B., Konopacky, Q. M., & Marois, C. 2011a, The Astrophysical Journal, 733, 65
—. 2011b, The Astrophysical Journal Letters, 735, L39
Bayo, A., Rodrigo, C., Barrado Y Navascués, D., et al. 2008, A&A, 492, 277, doi: 10.1051/0004-6361:200810395
Beuzit, J.-L., Vigan, A., Mouillet, D., et al. 2019, Astronomy & Astrophysics, 631, A155
Bohn, A., Kenworthy, M., Ginski, C., et al. 2020a, Monthly Notices of the Royal Astronomical Society, 492, 431
Bohn, A. J., Kenworthy, M. A., Ginski, C., et al. 2020b, The Astrophysical Journal Letters, 898, L16
Bonnefoy, M., Zurlo, A., Baudino, J.-L., et al. 2016, Astronomy & Astrophysics, 587, A58
Bowler, B. P., Liu, M. C., Dupuy, T. J., & Cushing, M. C. 2010, The Astrophysical Journal, 723, 850
Briesemeister, Z., Skemer, A. J., Stone, J. M., et al. 2018, in Ground-based and Airborne Instrumentation for Astronomy VII, Vol. 10702, International Society for Optics and Photonics, 107022Q
Charnay, B., Bézard, B., Baudino, J.-L., et al. 2018, The Astrophysical Journal, 854, 172
Chilcote, J., Pueyo, L., De Rosa, R. J., et al. 2017, The Astronomical Journal, 153, 182
Currie, T., Burrows, A., Itoh, Y., et al. 2011, The Astrophysical Journal, 729, 128
Currie, T., Burrows, A., Girard, J. H., et al. 2014, The Astrophysical Journal, 795, 133
Defrere, D., Absil, O., Hinz, P., et al. 2014, in Adaptive Optics Systems IV, Vol. 9148, International Society for Optics and Photonics, 91483X
Doelman, D. S., Por, E. H., Ruane, G., Escuti, M. J., & Snik, F. 2020, Publications of the Astronomical Society of the Pacific, 132, 045002
Doelman, D. S., Snik, F., Warriner, N. Z., & Escuti, M. J. 2017, in Techniques and Instrumentation for Detection of Exoplanets VIII, ed. S. Shaklan, Vol. 10400, International Society for Optics and Photonics (SPIE), 224 – 235, doi: 10.1117/12.2273406
Finger, G., Dorn, R. J., Eschbaumer, S., et al. 2008, in High Energy, Optical, and Infrared Detectors for Astronomy III, Vol. 7021, International Society for Optics and Photonics, 70210P
Fortney, J. J., Lodders, K., Marley, M. S., & Freedman, R. S. 2008, The Astrophysical Journal, 678, 1419
Galicher, R., Marois, C., Macintosh, B., Barman, T., & KONOPACkY, Q. 2011, The Astrophysical Journal Letters, 739, L41
GRAVITY Collaboration, Lacour, S., Nowak, M., et al. 2019, A&A, 623, L11, doi: 10.1051/0004-6361/201935253
Greenbaum, A. Z., Pueyo, L., Ruffio, J.-B., et al. 2018, The Astronomical Journal, 155, 226
Groff, T., Chilcote, J., Brandt, T., et al. 2017, in Techniques and Instrumentation for Detection of Exoplanets VIII, Vol. 10400, International Society for Optics and Photonics, 1040016
Haffert, S., Bohn, A., de Boer, J., et al. 2019, Nature Astronomy, 3, 749
Keppler, M., Benisty, M., Müller, A., et al. 2018, Astronomy & Astrophysics, 617, A44
Lagrange, A.-M., Gratadour, D., Chauvin, G., et al. 2009, Astronomy & Astrophysics,

493, L21
Larkin, J., Barczys, M., Krabbe, A., et al. 2006, New Astronomy Reviews, 50, 362
Lavie, B., Mendonça, J. M., Mordasini, C., et al. 2017, The Astronomical Journal, 154, 91
Lew, B. W., Apai, D., Marley, M., et al. 2020a, arXiv preprint arXiv:2009.10714
Lew, B. W., Apai, D., Zhou, Y., et al. 2020b, The Astronomical Journal, 159, 125
Macintosh, B., Graham, J. R., Ingraham, P., et al. 2014, proceedings of the National Academy of Sciences, 111, 12661
Macintosh, B., Graham, J., Barman, T., et al. 2015, Science, 350, 64
Madhusudhan, N., Burrows, A., & Currie, T. 2011, The Astrophysical Journal, 737, 34
Marley, M. S., Saumon, D., Cushing, M., et al. 2012, The Astrophysical Journal, 754, 135
Marois, C., Lafreniere, D., Doyon, R., Macintosh, B., & Nadeau, D. 2006, The Astrophysical Journal, 641, 556
Marois, C., Macintosh, B., Barman, T., et al. 2008, science, 322, 1348
Marois, C., Zuckerman, B., Konopacky, Q. M., Macintosh, B., & Barman, T. 2010, Nature, 468, 1080
Mawet, D., Wizinowich, P., Dekany, R., et al. 2016, in Adaptive Optics Systems V, Vol. 9909, International Society for Optics and Photonics, 99090D
Mollière, P., Wardenier, J., van Boekel, R., et al. 2019, Astronomy & Astrophysics, 627, A67
Mollière, P., Stolker, T., Lacour, S., et al. 2020, Astronomy & Astrophysics, 640, A131
Morzinski, K. M., Males, J. R., Skemer, A. J., et al. 2015, The Astrophysical Journal, 815, 108
Otten, G., Vigan, A., Muslimov, E., et al. 2020, arXiv preprint arXiv:2009.01841
Otten, G. P., Snik, F., Kenworthy, M. A., et al. 2017, The Astrophysical Journal, 834, 175
Por, E. H., Haffert, S. Y., Radhakrishnan, V. M., et al. 2018, in Adaptive Optics Systems VI, Vol. 10703, International Society for Optics and Photonics, 1070342
Racine, R., Walker, G. A., Nadeau, D., Doyon, R., & Marois, C. 1999, Publications of the Astronomical Society of the Pacific, 111, 587
Rajan, A., Rameau, J., De Rosa, R. J., et al. 2017, The Astronomical Journal, 154, 10
Samland, M., Mollière, P., Bonnefoy, M., et al. 2017, Astronomy & Astrophysics, 603, A57
Skemer, A. J., Hinz, P., Stone, J., et al. 2018, in Ground-based and Airborne Instrumentation for Astronomy VII, ed. C. J. Evans, L. Simard, & H. Takami, Vol. 10702, International Society for Optics and Photonics (SPIE), 78 – 85, doi: 10.1117/12.2314091
Skemer, A. J., Hinz, P. M., Esposito, S., et al. 2012, The Astrophysical Journal, 753, 14
Skemer, A. J., Marley, M. S., Hinz, P. M., et al. 2014, The Astrophysical Journal, 792, 17
Skemer, A. J., Hinz, P., Montoya, M., et al. 2015, in Techniques and Instrumentation for Detection of Exoplanets VII, Vol. 9605, International Society for Optics and Photonics, 96051D
Snik, F., Otten, G., Kenworthy, M., et al. 2012, in Modern Technologies in Space-and Ground-based Telescopes and Instrumentation II, Vol. 8450, International Society for Optics and Photonics, 84500M
Stolker, Bonse, M. J., Quanz, S. P., et al. 2019, A&A, 621, A59, doi: 10.1051/0004-6361/201834136
Stolker, T., Min, M., Stam, D. M., et al. 2017, Astronomy & Astrophysics, 607, A42

van Holstein, R. G., Snik, F., Girard, J. H., et al. 2017, in Techniques and Instrumentation for Detection of Exoplanets VIII, Vol. 10400, International Society for Optics and Photonics, 1040015

Wagner, K., Stone, J., Dong, R., et al. 2020, The Astronomical Journal, 159, 252

Wang, J., Wang, J., Ma, B., et al. 2020, arXiv preprint arXiv:2007.02810

Wilson, J. C., Hinz, P. M., Skrutskie, M., et al. 2008, in Optical and Infrared Interferometry, Vol. 7013, International Society for Optics and Photonics, 70133A